Article

Structural transitions, octahedral rotations, and electronic properties of $A_3Ni_2O_7$ rare-earth nickelates under high pressure

Check for updates

Benjamin Geisler [1,2] ✉, James J. Hamlin[1], Gregory R. Stewart[1], Richard G. Hennig[2,3] & P. J. Hirschfeld[1]

Motivated by the recent observation of superconductivity with $T_c \sim 80$ K in pressurized $La_3Ni_2O_7$[1], we explore the structural and electronic properties of $A_3Ni_2O_7$ bilayer nickelates (A = La-Lu, Y, Sc) as a function of pressure (0–150 GPa) from first principles including a Coulomb repulsion term.
At ~ 20 GPa, we observe an orthorhombic-to-tetragonal transition in $La_3Ni_2O_7$ at variance with x-ray diffraction data, which points to so-far unresolved complexities at the onset of superconductivity, e.g., charge doping by variations in the oxygen stoichiometry. We compile a structural phase diagram that establishes chemical and external pressure as distinct and counteracting control parameters. We find unexpected correlations between T_c and the *in-plane* Ni-O-Ni bond angles for $La_3Ni_2O_7$. Moreover, two structural phases with significant c^+ octahedral rotations and in-plane bond disproportionations are uncovered for A = Nd-Lu, Y, Sc that exhibit a pressure-driven electronic reconstruction in the Ni e_g manifold. By disentangling the involvement of basal versus apical oxygen states at the Fermi surface, we identify $Tb_3Ni_2O_7$ as an interesting candidate for superconductivity at ambient pressure. These results suggest a profound tunability of the structural and electronic phases in this novel materials class and are key for a fundamental understanding of the superconductivity mechanism.

The discovery of superconductivity in Sr-doped infinite-layer $NdNiO_2$ films grown on $SrTiO_3(001)$[2–4] introduced a new class of formally Ni^{1+} ($3d^9$) cuprate-like superconductors[5–27]. Subsequent work rapidly increased the family of superconducting nickelate compounds, for instance, to $PrNiO_2$ and $LaNiO_2$ films[28,29] as well as to quintuple Ruddlesden-Popper-derived films[30]. While epitaxial strain constitutes a successful and well-established route to realize novel quantum phases in rare-earth nickelates[31–34], the impact of extreme pressure conditions is far less explored. Intriguingly, a pressure-driven increase of the superconducting transition temperature T_c in Sr-doped infinite-layer $PrNiO_2$ has been measured[35].

Very recently, signatures of superconductivity with a high $T_c \sim 80$ K were reported in the bilayer nickelate $La_3Ni_2O_7$ subject to ~14–43.5 GPa external pressure in a diamond anvil cell[1]. This structure is a member of the Ruddlesden-Popper family, $A_{n+1}Ni_nO_{3n+1}$ ($n = 2$), and contributes another exciting perspective to this field, specifically due to the formal valence of $Ni^{2.5+}$. Independent experimental works have already claimed confirmation

of high-temperature superconductivity in this system in a similar pressure range[36,37].

This observation instantly spurred a sizable amount of initial theoretical literature on $La_3Ni_2O_7$[38–55]. The general superconductivity mechanism that has been put forward involves a pressure-driven transition of the Fermi surface topology, featuring an emerging hole pocket of Ni $3d_{z^2}$ character[1,38–41,50,52]. This typically results in a superconducting pairing with leading $s^\pm$ eigenvalue[39,40,50–52], rendering the bilayer nickelates distinct from cuprates[56] and Fe-based superconductors[57]. This electronic transition is believed to be accompanied by a structural transition from a $Cmcm$ (or $Amam$; space group No. 63) to a $Fmmm$ (No. 69) phase, *both* orthorhombic[1], with a concomitant suppression of the NiO_6 octahedral tilts that are characteristic of the $Cmcm$ phase.

This raises the fundamental questions (i) how the structural transition and the accompanying lack of octahedral rotations are related to the emergence of superconductivity, and (ii) if we can reduce the critical

[1]Department of Physics, University of Florida, Gainesville, FL 32611, USA. [2]Department of Materials Science and Engineering, University of Florida, Gainesville, FL 32611, USA. [3]Quantum Theory Project, University of Florida, Gainesville, FL 32611, USA. ✉e-mail: benjamin.geisler@ufl.edu

pressure by chemical precompression (a key concept in superconducting hydrides[58,59]) via isoelectronic A-site variation. In oxides, octahedral rotations are known to be sensitively related to the electronic structure and the degree of electronic correlation: In the isomorphic bilayer compound $Sr_3Ru_2O_7$, for example, similar octahedral rotations of around $\sim 6°$[60,61] are suppressed by Mn doping, which drives the emergence of antiferromagnetic order[60,62,63] and a low-temperature Mott insulating phase[64,65]. Thus, the avoidance of octahedral relaxations may be coupled to unconventional superconductivity, although the exact mechanism remains elusive.

Here we provide a comprehensive and consistent exploration of the structural and electronic properties in $A_3Ni_2O_7$ bilayer nickelates (A = La-Lu, Y, Sc) as a function of hydrostatic pressure (0–150 GPa) from first principles including a Coulomb repulsion term. We compile a structural phase diagram with particular emphasis on the orthorhombic distortion (b/a ratio), octahedral anisotropy, and octahedral rotations. Surprisingly, chemical and external pressure emerge as two distinct and counteracting control parameters, which limits the perspectives of chemical precompression in this system. We trace this phenomenon back to the enhancement of octahedral rotations with reducing A-site ionic radius. The response of the lattice parameters to external pressure is found to be highly anisotropic. In $La_3Ni_2O_7$ at ~ 20 GPa, we observe an orthorhombic-to-tetragonal transition to an $I4/mmm$ phase at variance with recent x-ray diffraction (XRD) data, which points to yet unresolved complexities near the onset of superconductivity, e.g., electron- or hole-doped samples due to variations in the oxygen stoichiometry, and suggests a careful reassessment

of the so-far proposed superconductivity mechanisms. The critical pressure associated with this transition, which coincides universally with vanishing octahedral tilts, is found to increase quadratically over the rare-earth series. For A = Nd-Lu, Y, Sc, two structural phases are uncovered at ambient conditions that are characterized by the emergence of significant in-plane c^+ octahedral rotations as well as in-plane bond disproportionations and exhibit a surprising pressure-driven electronic reconstruction involving the rotation of the Ni d_{z^2} orbital. The successive quenching of the distinct rotational degrees of freedom by pressure demonstrates that the potential energy landscape of the in-plane octahedral rotations is significantly shallower than for the octahedral tilts. Moreover, we highlight unexpected correlations between T_c and the *in-plane* Ni-O-Ni bond angles for $La_3Ni_2O_7$ and discuss their possible relation to superconductivity. Finally, by disentangling the involvement of basal versus apical oxygen ions in the Fermi surface, we identify $Tb_3Ni_2O_7$ as an interesting candidate for superconductivity at ambient pressure.

Results
Structural phase diagram of $A_3Ni_2O_7$ rare-earth nickelates under high pressure
Over the rare-earth series and the considered pressure range ($p = 0$–150 GPa), we observe an unexpected richness of the structural properties of $A_3Ni_2O_7$ (Fig. 1). Our comprehensive study puts us in position to compile an ab initio structural phase diagram [Fig. 1d], which underlines the possible potential of high-pressure experiments to realize exotic new
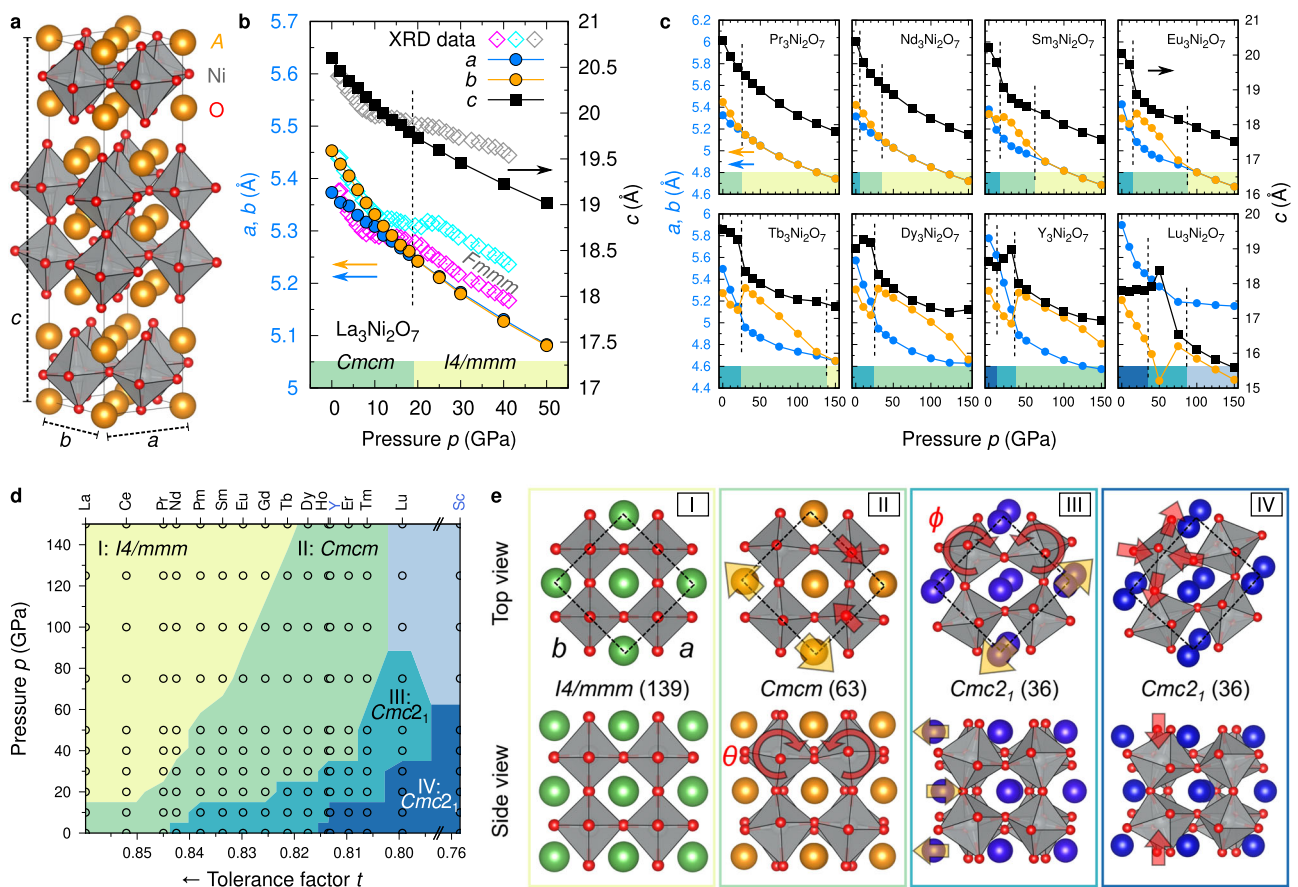

Fig. 1 | Structural properties of $A_3Ni_2O_7$ rare-earth nickelates under high pressure. a Structure of the bilayer Ruddlesden-Popper nickelate $A_3Ni_2O_7$. **b** Lattice parameter analysis for $La_3Ni_2O_7$ as a function of the external pressure p. While our DFT + U predictions agree closely with experimental observations[1] for low pressure, we observe an unexpected transition to a tetragonal $I4/mmm$ ($a = b$) instead of an orthorhombic $Fmmm$ phase ($a \neq b$) around $p \sim 20$ GPa. **c** Lattice parameters for selected $A_3Ni_2O_7$ nickelates. The vertical dashed lines mark structural phase

boundaries. **d** Structural phase diagram for $A_3Ni_2O_7$, contrasting the impact of chemical versus external pressure. It has been compiled from the DFT + U data discussed in Figs. 2 and 3 (marked by small circles). **e** Corresponding top and side views of representative bilayer slabs. The arrows mark characteristic differences between the distinct structural phases, involving octahedral rotations ϕ and tilts θ, distinct orthorhombic distortions b/a, typical displacements of the A-site ions, and different bond disproportionations of the NiO_6 octahedra.
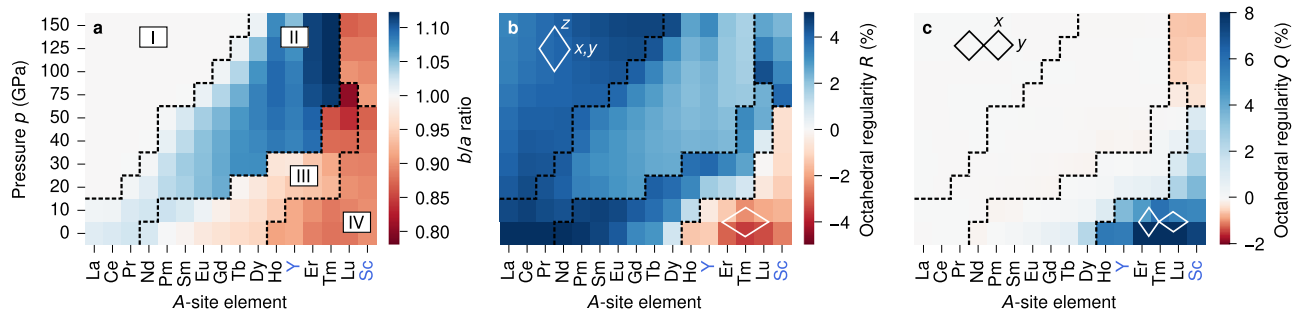
Fig. 2 | Structural trends of $A_3Ni_2O_7$ across the rare-earth series (including Y and Sc) for varying external pressure p from 0 to 150 GPa. The A-site elements are ordered according to their ionic radius. The dashed lines separate the distinct structural phases [Fig. 1d]. **a** The b/a ratio clearly identifies the tetragonal $I4/mmm$ phase I and separates it from the $Cmcm$ phase II with $b/a > 1$. The remaining phases show largely $b/a < 1$. **b** Apical versus basal extension of the octahedra (R). In phases I–III, the octahedra are elongated in vertical $z \sim c$ direction, particularly for $La_3Ni_2O_7$ at ambient conditions. In contrast, phase IV exhibits vertically compressed octahedra. **c** The in-plane disproportionation of the O-Ni-O distances (Q) is very pronounced in phase IV, which is characterized by cigar-shaped octahedra alternating in the plane, reminiscent of $LaMnO_3$, and a considerable electronic reconstruction of the Ni $3d_{z^2}$ orbital.

quantum states in the bilayer nickelates in particular and in correlated transition metal oxides in general. In the following, we explore the phase diagram and the underlying data step by step and discuss their implications for superconductivity.

Pressure-induced orthorhombic-to-tetragonal transition in $La_3Ni_2O_7$

We begin by analyzing the pressure dependence of the lattice parameters of $La_3Ni_2O_7$ [Fig. 1a, b]. The fully ab initio relaxed results for a, b and c agree closely with the experimental lattice parameters refined from XRD[1] between 0 and 10 GPa. In particular, the difference between a and b (orthorhombic distortion) is accurately captured. This further corroborates that the Hubbard $U = 3$ eV employed here is appropriate. Consistent with previous experimental[66,67] and theoretical assessments[1,52], we identify a $Cmcm$ structure at low pressure, referred to as phase II in the following [Fig. 1d]. It is characterized by finite octahedral tilts θ and $b/a > 1$, where we define b as the axis along which the tilts are expressed [Fig. 1e]. Simultaneously, octahedral rotations in the basal plane are absent ($\phi = 0$, c^0). Notably, without any octahedral rotations ($Fmmm$, $I4/mmm$), the assignment of a and b is arbitrary.

Between 10 and 20 GPa, the experimental lattice parameters a and b display the unambiguous trend to converge, accompanied by a plateau in the c curve. However, a sudden increase can be observed at ~ 20 GPa, after which they continue to decrease monotonically with a finite separation of around 0.075 Å. It has been suggested earlier that the octahedral tilts are quenched in this pressure range ($\theta = 0$), corresponding to inter-layer Ni-O-Ni bond angles of 180° and resulting in an orthorhombic $Fmmm$ geometry[1]. This structure was explored in detail in subsequent work[38,40–42,44,45,47,48,50,52].

Surprisingly, we observe a clear orthorhombic-to-tetragonal transition at $p \sim 20$ GPa, resulting in a structure of $I4/mmm$ symmetry (phase I, space group No. 139) rather than the so-far reported $Fmmm$ geometry. The enthalpy difference between the $Fmmm$ (lattice parameters from XRD[1]) and the $I4/mmm$ geometry obtained here, exemplarily for $La_3Ni_2O_7$ at 30 GPa, amounts to $\Delta H = 90$ meV/Ni, which additionally corroborates our findings. Moreover, we confirmed the orthorhombic-to-tetragonal transition by variation of U at the Ni site, additional application of U to the La $4f$ and $5d$ states, and different patterns of the octahedral rotations (c^0, c^+, c^-). We recently became aware of higher-resolution x-ray experiments that report the observation of the $I4/mmm$ phase above $p \sim 19$ GPa[68].

We demonstrate below for $La_3Ni_2O_7$ that the key features of the electronic structure are preserved between the $I4/mmm$ and $Fmmm$ phases. Nevertheless, these observations suggest so-far unresolved complexities at the onset of superconductivity which may be key in identifying the underlying mechanism: On the one hand, the application of pressure may not be uniform, as indicated by the role of different pressure-transmitting media employed in the diamond anvil cells[1,36,37]. On the other hand, these results may indicate that the experimental samples are electron or hole

doped, most probably due to variations in the oxygen stoichiometry. There is considerable evidence that the electronic properties are extremely sensitive to small changes in the oxygen vacancy concentration[66,69]. Due to the strong coupling of the charge and lattice degrees of freedom in correlated transition metal oxides[70–74], this would alter their structural response to pressure and potentially lead to the experimentally observed finite orthorhombic distortion at higher pressure. In that case, the so-far proposed $s^\pm$ superconductivity mechanism needs a careful reassessment.

Can we substitute external by chemical pressure?

Next, we explore the role of chemical pressure by isoelectronic variation of the A-site element. The ionic radii range from 1.172 (La^{3+}) to 1.001 (Lu^{3+}), as well as 1.04 (Y^{3+}) and 0.885 (Sc^{3+}). We represent this chemical pressure by the Goldschmidt tolerance factor:

$$t(A) = \frac{r_A + r_O}{\sqrt{2}\,(r_{Ni} + r_O)} \; , \tag{1}$$

where $t = 1$ corresponds to size-balanced A and Ni sites. It is reasonable to order the A-site elements with decreasing t [Fig. 1(d)]. Here we find consistently $t < 1$. Can we exploit this strategy to lower the critical external pressure driving the structural phase transition and thus facilitate the emergence of superconductivity in the bilayer nickelates?

We can directly conclude from the phase diagram in Fig. 1d, which is not symmetric, that this hypothesis does not hold. The transition from the $Cmcm$ to the $I4/mmm$ phase occurs at a critical pressure that increases monotonically from $p \sim 20$ ($A =$ La, Ce), 30 (Pr), and 40 GPa (Nd) to $p \sim 125$–150 GPa (Tb), with a parabola-shaped phase boundary as a function of t [see also the b/a ratios in Fig. 2a and the octahedral tilts θ in Fig. 3a]. While finalizing this manuscript, we became aware of another very recent work that suggests a similar shape of this phase boundary, albeit classifying the high-pressure phase as $Fmmm$[75]. If superconductivity is linked to this structural phase transition, our results imply that continuously increasing external pressures are required as A progresses through the rare-earth series. In the following, we will identify enhanced octahedral rotations as the impeding physical mechanism.

These results unambiguously show that chemical and external pressure constitute two distinct control parameters that independently and non-interchangeably allow the designing of the quantum state in bilayer rare-earth nickelates.

Anisotropic pressure response of the lattice parameters

Figure 1c shows that the cell height c varies overall from ~15 ($A =$ Sc at 150 GPa) to 20.6 Å (La at 0 GPa) and generally reduces with decreasing ionic radius of the A-site element. Some pronounced discontinuities can be observed at the phase boundaries, e.g., between phases II and III [Fig. 1c].
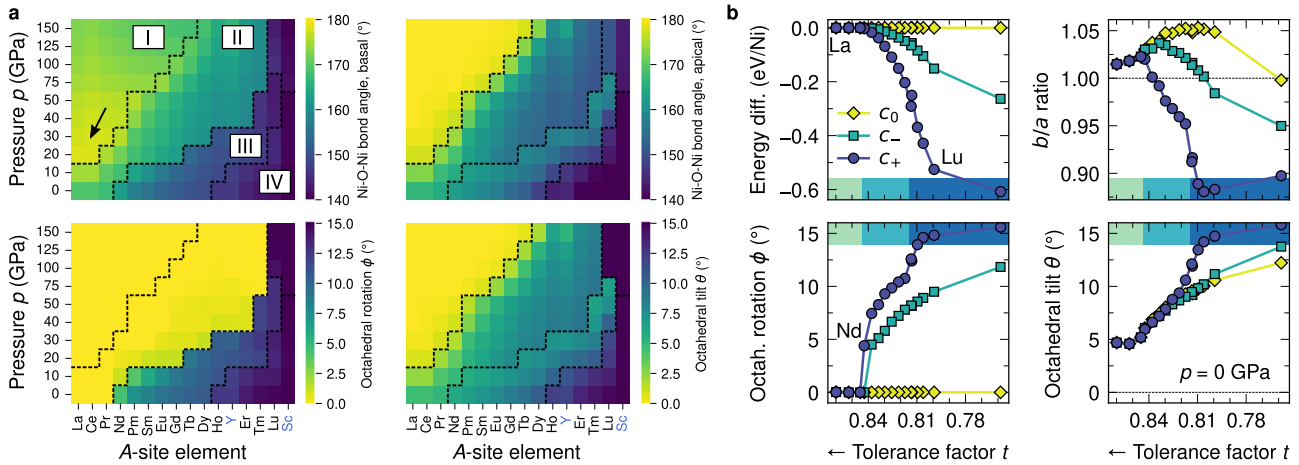
Fig. 3 | Analysis of the Ni-O-Ni bond angles and octahedral rotations in $A_3Ni_2O_7$. a Impact of chemical versus external pressure. The dashed lines separate the distinct structural phases [Fig. 1d]. Surprisingly, we observe an overall maximum in the *in-plane* Ni-O-Ni bond angles for A = La at 20 GPa, i.e., near the experimental onset of superconductivity (marked by the arrow). For higher pressure, the in-plane bond angles are enhanced again, which correlates with the experimentally observed reduction of T_c. **b** Detailed perspective at the in-plane octahedral rotations ϕ in $A_3Ni_2O_7$ at $p = 0$ GPa. While absent for A = La-Pr, ferrodistortive c^+ rotations stabilize for Nd-Lu, Y, Sc and induce a reversal from $b/a > 1$ to $b/a < 1$. Moreover, they couple strongly to the octahedral tilts θ and enhance them considerably for the later rare-earth compounds ($t < 0.82$).

Surprisingly, a counter-intuitive *increase* of c can be identified with increasing pressure for ~ 0–50 GPa in $Dy_3Ni_2O_7$, $Y_3Ni_2O_7$, and $Lu_3Ni_2O_7$ (phase III).

For the in-plane lattice parameters a and b, which range from 4.41 (A = Sc at 150 GPa) to 5.95 Å (Tm at 0 GPa), a simple decreasing A-site dependence can only be identified for the early rare-earth metals up to Nd [Fig. 1c]. Between Pm and Tm, even a sharp upturn in the average of a and b can be observed, which also translates to the basal Ni-Ni distances (not shown).

This coincides with the stabilization of the novel structural phases III and IV [Fig. 1d]. Both have $Cmc2_1$ symmetry (space group No. 36) and are characterized by finite ferrodistortive (c^+) octahedral rotations arising as an additional degree of freedom ($\phi > 0$; Fig. 3). These are accompanied by substantial A-site displacements in the basal plane [Fig. 1e], which are typical for this octahedral rotation pattern[73,74] and a useful fingerprint in transmission electron microscopy. The transition to the $Cmcm$ phase II is associated with pronounced jumps of a and b [Fig. 1c], resulting generally in a reversal of the b/a ratio [Fig. 2a].

We see that the response of the lattice parameters to uniform external pressure is highly anisotropic. The cell height c is generally compressed more strongly than a and b. This can be traced back to a partial accommodation of the pressure by the more elastic bilayer separation. For example, we find that the latter reduces from 6.4 to 5.34 Å for 0–150 GPa in $La_3Ni_2O_7$, which clearly exceeds the concomitant compression of the bilayer height from 3.91 to 3.54 Å (each measured between the Ni planes).

Inspection of the phase diagram in Fig. 1d reveals that the boundaries between phases II–III and III–IV are roughly parabola-shaped as a function of t, similar to the boundary between phases I–II. This further corroborates the opposing impact of external pressure versus A-site variation. Beyond the phases I–IV [top-right corner of Fig. 1d], we found that these counteracting forces lead to bizarre deformations of the NiO_6 octahedra (not shown), which indicates that the compounds become unstable under such extreme conditions.

The richness of the structural phase diagram and the unexpected transitions identified in the later rare-earth nickelates provide additional opportunities for e.g. superconducting phases. We will shed more light on this aspect below.

Octahedral anisotropy and bond disproportionation
The anisotropic pressure response of the lattice parameters is directly related to shape modifications of the NiO_6 octahedra, which in turn determine the spatial orientation of the two Ni e_g orbitals and their relative occupation, i.e., the orbital polarization[76–78]. We measure the deviations from an ideal, regular octahedron by defining

$$R = \frac{d_z - d_{x,y}}{d_z + d_{x,y}} \quad \text{and} \quad Q = \frac{d_x - d_y}{d_x + d_y} \quad (2)$$

from the in-plane O-Ni-O distances d_x and d_y (which may alternate among the Ni sites in a checkerboard pattern, resulting in $Q \neq 0$), their average $d_{x,y}$, and the out-of-plane O-Ni-O distances d_z.

The octahedral anisotropy R is a measure of the apical versus basal extension of the octahedra [Fig. 2b]. It ranges overall from 5.3% (A = La at 0 GPa) to − 3.5% (Tm at 0 GPa). We find $R > 0$ for most rare-earth nickelates, implying an elongation of the Ni octahedra in the $z \sim c$ direction and thus a Ni d_{z^2} orbital that points in the apical direction, whereas the Ni $d_{x^2-y^2}$ orbital is oriented in the basal plane.

Notably, the broken octahedral connectivity between the bilayer slabs results in an internal asymmetry of each NiO_6 octahedron, visible in the structural side views in Fig. 1e. Specifically, for $La_3Ni_2O_7$, the Ni-O bond lengths involving the 'outer' apical oxygen ions (pointing into the structural gap) are generally enhanced[1,41]. Simultaneously, we find that these Ni-O bonds are reduced more strongly due to pressure than their 'inner' analogs. For instance, we observe 2.31, 1.97 Å (0 GPa), 2.08, 1.90 Å (30 GPa), and 1.91, 1.81 Å (100 GPa) for the outer and inner apical Ni-O bonds, respectively. This mechanism facilitates the vertical elongation of the octahedra and thus the occupation of the Ni d_{z^2} orbital.

The early rare-earth elements exhibit a monotonically decreasing trend of R with increasing pressure, i.e., the anisotropy is reduced [Fig. 2b]. This is in line with the more rapid decrease of c with respect to a and b. Specifically, for $La_3Ni_2O_7$, we find that R decreases from 5.3% at 0 GPa to 3.3% at 150 GPa. The central rare-earth elements exhibit a more complex pressure dependence [Fig. 2b]. Sharp discontinuities at the phase transition II–III can be observed, and correlations with the orthorhombic distortion (b/a ratio) are clearly visible, particularly in phase II [Fig. 2a].

At zero pressure, R decreases rapidly over the rare-earth series [Fig. 2b]. Intriguingly, it becomes negative for A = Ho-Lu, Y, Sc, which corresponds to vertically compressed octahedra (phase IV). The respective compounds show a pressure-induced transition from $R < 0$ to $R > 0$ at critical pressures ranging from ~ 10 to 75 GPa. This behavior is highly distinct from all other bilayer rare-earth nickelates.
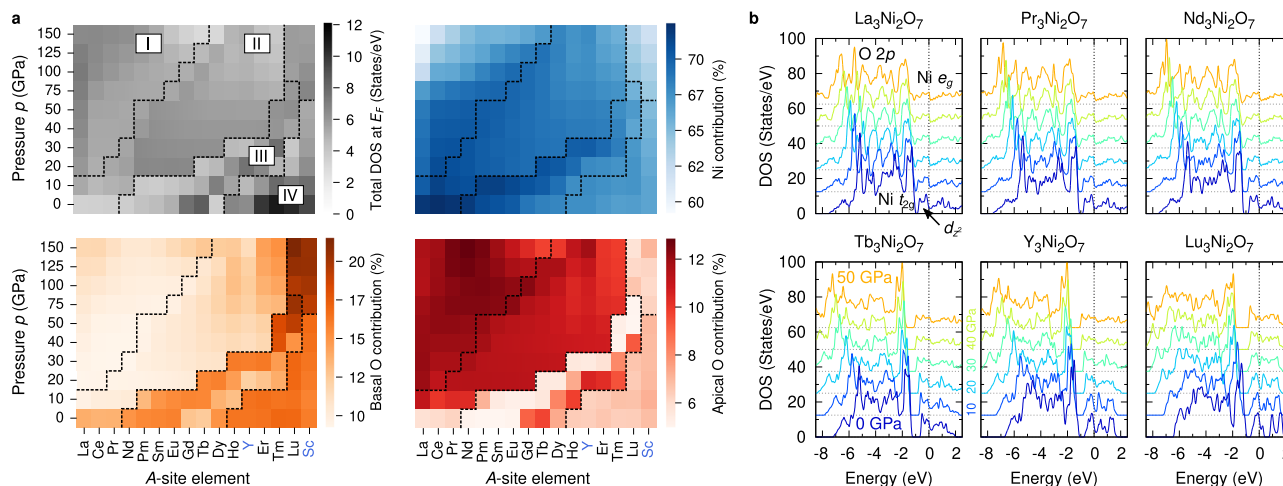
Fig. 4 | Electronic structure of $A_3Ni_2O_7$ rare-earth nickelates. a Total DOS at the Fermi energy and relative contributions from the Ni, basal oxygen, and apical oxygen ions. The dashed lines separate the distinct structural phases [Fig. 1d]. Noteworthy are the high contributions from the apical oxygen ions in phases I and II. Intriguingly, $Tb_3Ni_2O_7$ at zero pressure presents a considerably higher DOS at the Fermi level (~8.5 States/eV) than $La_3Ni_2O_7$ reaches at around 100 GPa (~7.2 States/eV) in addition to a sizable involvement of the apical oxygen ions. **b** Evolution of the total DOS as a function of the external pressure from 0 (blue) to 50 GPa (orange) for selected compounds. An overall pressure-induced broadening of the O $2p$-derived valence band can be observed, as well as of the Ni e_g manifold located at the Fermi energy. Characteristic peaks clearly shift to lower energies, e.g., the Ni t_{2g} peak visible between -2 and -1 eV at zero pressure, or the oxygen peak around -5.5 eV (A = La-Tb). The feature directly below the Fermi energy (marked by the arrow) corresponds to the lower set of Ni $3d_{z^2}$-O $2p_z$ hybrid states [Fig. 5a].

Figure 2c quantifies the in-plane disproportionation of the O-Ni-O distances (Q). We observe that it vanishes in phases I and II. In phase III, where $R > 0$, typical values are finite but small, e.g., -0.06% (A = Nd) and 0.79% (Tb) at zero pressure. Surprisingly, Q becomes very pronounced in phase IV, which coincides with $R < 0$, and reaches 9% at A = Tm at zero pressure. This corresponds to cigar-shaped octahedra that alternate in the plane in conjunction with c^+ octahedral rotations (Fig. 3), a pattern that closely resembles $LaMnO_3$[79,80]. Most importantly, this coincides with a considerable electronic reconstruction involving the rotation of the Ni d_{z^2} orbital into the basal plane. Intriguingly, we see that this phase can be lifted by pressure of around 10–40 GPa [Fig. 2c]. Such extreme tunability of the geometry and the electronic structure is highly promising and deserves further exploration.

The pivotal role of octahedral rotations

Figure 3a analyzes the basal and apical Ni-O-Ni bond angles as well as the octahedral rotations ϕ and tilts θ [defined in Fig. 1e] in $A_3Ni_2O_7$, which provide insightful and distinct perspectives on the rotational degrees of freedom.

In the $Cmcm$ phase II, where $\phi = 0$, we find that θ ranges from ~2 to 8°. In the $Cmc2_1$ phases III and IV, ϕ and θ are both enhanced to ~4–15°. With increasing pressure, the in-plane rotations ϕ, if present, are quenched first (for A = Nd-Tm at 10–75 GPa), which corresponds to the boundary between phases II and III. For Lu and Sc, the octahedral rotations are so pronounced that we observe finite values up to 150 GPa. Subsequently, the octahedral tilts θ are quenched at yet higher pressure values (for A = La-Tb at 20–150 GPa). Intriguingly, we find that these vanishing tilts coincide universally with the orthorhomic-to-tetragonal transition from phase II to phase I.

This demonstrates that external pressure generally reduces or even quenches the octahedral rotations, whereas chemical pressure rather enhances them. The consecutive suppression of the distinct rotational degrees of freedom indicates that different energy scales are involved, with a significantly shallower potential energy landscape related to ϕ than to θ.

The superconducting transition has been so far associated with a straightening of the inter-layer (apical) Ni-O-Ni bond angles towards 180°[1]. The respective top-right panel in Fig. 3a closely resembles the bottom-right panel displaying the octahedral tilts θ and shows that pressures up to 150 GPa successfully engineer this state for A = La-Tb. In particular, ~20 GPa for $La_3Ni_2O_7$ are sufficient to obtain inter-layer Ni-O-

Ni bond angles close to 180°. For $Ce_3Ni_2O_7$, already slightly lower pressures result in this state, whereas $Pr_3Ni_2O_7$ and $Nd_3Ni_2O_7$ require rather ~30–40 GPa. At zero pressure, we observe a value of 168° for $La_3Ni_2O_7$, in perfect agreement with previous work[1]. The late rare-earth nickelates exhibit considerably smaller values (i.e., more pronounced bond angles), reaching even below 140° for Lu and Sc.

Motivated by the superconducting infinite-layer nickelates, which exhibit *in-plane* Ni-O-Ni bond angles of 180°[2,10,19,21], we additionally explore these quantities for the bilayer nickelates. They directly impact the basal Ni $3d_{x^2-y^2}$-O $2p_{x,y}$ hybridization and thus the electronic structure at the Fermi energy [see also Fig. 4a below] including the Ni e_g orbital polarization as well as possible superexchange mechanisms. Intriguingly, the comprehensive perspective provided in Fig. 3a, top-left panel, unveils an overall maximum for A = La at 20 GPa, i.e., close to the experimental onset of superconductivity. For higher pressure, the in-plane bond angles are enhanced again, which we find to surprisingly correlate with the experimentally observed reduction of T_c[1,36,37]. It is important to note here that the in-plane Ni-O-Ni bond angles can deviate from 180° *despite* $\theta = \phi = 0$, since the basal oxygen ions show an increasing tendency towards a uniform inwards relaxation under high pressure that does not correspond to finite octahedral rotations. These observations suggest that the *in-plane* Ni-O-Ni bond angles are an important aspect in understanding the superconducting phase in bilayer rare-earth nickelates.

Figure 3b analyzes the structural impact of the in-plane octahedral rotations ϕ in $A_3Ni_2O_7$ at zero pressure, i.e., highlighting the chemical effect of A-site variation. While absent for A = La-Pr, ferrodistortive c^+ rotations stabilize for A = Nd-Lu, including Y and Sc, with a considerable energy difference $\Delta E \sim -0.6$ eV/Ni relative to the metastable c^0 case. We see that they are strongly coupled to the b/a ratio and induce a reversal from $b/a > 1$ to $b/a < 1$, which for antiferrodistortive c^- rotations occurs only for Lu and Sc and without octahedral rotations (c^0) only for Sc. Moreover, they couple strongly to the octahedral tilts θ and enhance them considerably for the later rare-earth nickelates (phase IV, $t < 0.82$), an effect that is clearly absent for c^- and c^0. This demonstrates that a correct description of the octahedral rotations is key to obtain accurate structural properties for A = Nd-Lu, Y, Sc.

Electronic structure of $A_3Ni_2O_7$ rare-earth nickelates under high pressure

Finally, we explore how the structural observations we discussed above relate to the electronic properties of $A_3Ni_2O_7$ rare-earth nickelates. Figure 4a
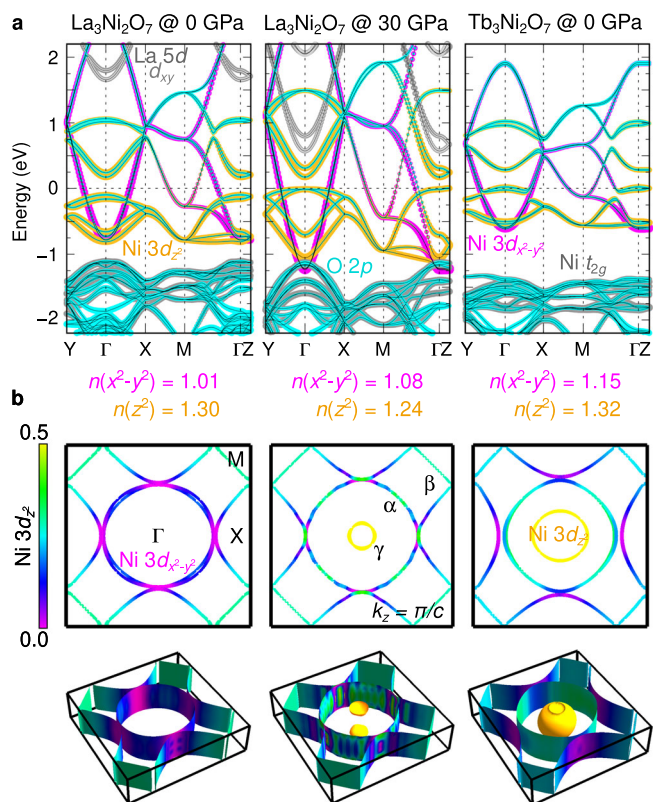
Fig. 5 | Electronic structure of La$_3$Ni$_2$O$_7$ at 0 GPa (*Cmcm*) and 30 GPa (*I4/mmm*) as well as Tb$_3$Ni$_2$O$_7$ at 0 GPa (*Cmc2$_1$*). a Band structures from DFT+U. The band character is represented by the different colors, and the Ni e_g occupation numbers n are explicitly provided. **b** The corresponding Fermi surfaces unravel an increase in Ni $3d_{z^2}$ orbital weight (color bar) in pressurized La$_3$Ni$_2$O$_7$, specifically for sheet α, and an emerging hole pocket (γ) around the Γ point. Tb$_3$Ni$_2$O$_7$ presents a similar Fermi surface topology at zero pressure, despite finite octahedral rotations, in conjunction with a considerably enhanced DOS at the Fermi energy [Fig. 4a].

displays the total density of states (DOS) at the Fermi energy as a function of the A-site element and the external pressure, which is an important indicator for enhanced superconducting properties. Furthermore, Fig. 4a disentangles the relative contributions from the Ni, basal oxygen, and apical oxygen ions. This allows us to track the composition of the Fermi surface, particularly variations in the basal versus apical oxygen involvement, which also reflects the Ni $3d_{x^2-y^2}$ versus $3d_{z^2}$ contributions, respectively.

Substantial correlations of all four panels with the distinct structural phases established above can be identified. Along the transition from phase III to II, as well as for A = La-Pr at ~ 10 GPa, we observe a sudden enhancement in the total DOS from roughly 3.5 to 6.5 States/eV. This is accompanied by a reduction of the basal oxygen contributions from ~ 15% to 10%, corresponding to the Ni $3d_{x^2-y^2}$-O $2p_{x,y}$ system, and a concomitant increase of the apical oxygen contributions from ~ 5% to 11%, related to the Ni $3d_{z^2}$-O $2p_z$ hybrid states. Simultaneously, the *absolute* Ni contributions increase as well, even though we see a slight reduction of the *relative* Ni contributions, which implies that the overall relevance of oxygen increases.

It is surprising that the enhanced involvement of apical oxygen clearly correlates with phase II ($\phi \sim 0$) rather than with phase I ($\theta \sim 0$). Nevertheless, within phase I, the apical oxygen contribution is generally further boosted and reaches its maximum > 12% for Nd at 150 GPa. In sharp contrast, in phase III and particularly IV the *basal* ions dominate the oxygen contributions to the Fermi surface. An exception are the unexpectedly high apical oxygen contributions arising along the transition from phase III to IV, i.e., at the verge to the strongly bond-disproportionated state which is accompanied by in-plane Ni $3d_{z^2}$ orbital order and vertically compressed octahedra discussed above [Fig. 2b, c].

The total DOS in La$_3$Ni$_2$O$_7$ ranges from ~ 3.5 States/eV at 0 GPa to ~7.2 States/eV at 100 GPa. By screening the A-site elements at $p = 0$ GPa, we identify even higher values particularly for Tb$_3$Ni$_2$O$_7$ (~8.5 States/eV). This compound also exhibits the characteristic reversal from basal to apical oxygen involvement that usually appears exclusively under finite pressure. The maximum of the total DOS is observed for Tm$_3$Ni$_2$O$_7$ at 0 GPa. However, the contributions from the Ni and the apical oxygen ions are relatively low for this compound, and its band structure (not shown) differs considerably from that of e.g. La$_3$Ni$_2$O$_7$ due to the Ni e_g electronic reconstruction.

Figure 4b tracks the evolution of the total DOS as a function of the external pressure for a selection of representative compounds. We observe an overall pressure-induced broadening of the O $2p$-derived valence band. Characteristic peaks are clearly shifted to lower energies with increasing pressure, e.g., the Ni t_{2g} peak visible between −2 and −1 eV at 0 GPa, and, even more strongly, the oxygen peak visible between − 4.5 and − 5.5 eV at 0 GPa.

The Ni e_g manifold is located around the Fermi energy. We see that its band width is considerably reduced across the rare-earth series, whereas finite external pressure broadens it. This observation reflects once again the counteracting nature of these two control parameters. The feature directly below the Fermi level has Ni $3d_{z^2}$-O $2p_z$ character [see also Fig. 5a]. Figure 4b demonstrates the pressure-induced occupation of these states for A = La, Pr, and Nd. Surprisingly, for Tb$_3$Ni$_2$O$_7$, we observe that they are already partly occupied at 0 GPa.

Finally, the DOS of Y$_3$Ni$_2$O$_7$ and Lu$_3$Ni$_2$O$_7$ has a distinct shape around the Fermi energy since the Ni $3d_{z^2}$ orbital is oriented in the plane at 0 GPa (phase IV), as we discussed above in the context of Fig. 2c. It is interesting to follow the evolution of these curves as pressure drives the structural transition to phase III, which uncovers a concomitant electronic reconstruction in the e_g manifold, i.e., a realignment of the Ni $3d_{z^2}$ orbital with the vertical axis. The high apical oxygen values at the phase boundary render this transition even more compelling, and A = Ho at ~ 10 GPa as well as A = Y-Tm at ~ 20 GPa emerge as further candidates for future in-depth exploration.

Figure 5a shows for the prototypical La$_3$Ni$_2$O$_7$ system that the Ni $3d_{z^2}$ bands are split into an occupied lower and an empty upper set, separated by a band gap of ~ 0.25 eV at 0 GPa. Simultaneously, the system is metallic due to highly dispersed Ni $3d_{x^2-y^2}$ states. Both Ni e_g orbitals hybridize substantially with each other around the M point[38] and, in addition, present an overall hybridization with the O $2p$ states.

Application of external pressure enhances the energy difference between the two Ni $3d_{z^2}$ sets, but simultaneously also the band width of the $3d_{x^2-y^2}$ and $3d_{z^2}$ states, which results in a reduction of the band gap. Moreover, the lower $3d_{z^2}$ set crosses the Fermi energy, and a fraction of its charge is transferred to the $3d_{x^2-y^2}$ bands. Thus, a 'self-doping' hole pocket around the Γ point appears [Fig. 5b; folded back from the M point of the primitive cell][1,38–41,50,52], which plays a key role in the suggested $s^\pm$ superconductivity mechanism[39,40,50–52]. We furthermore see an increase in Ni $3d_{z^2}$ orbital weight specifically in the α Fermi sheet. Notably, the Fermi surface of pressurized $I4/mmm$ La$_3$Ni$_2$O$_7$ strongly resembles previous reports based on the *Fmmm* geometry. Thus, moderate orthorhombic distortions rather impact details of the electronic structure.

The reduction of the octahedral anisotropy R with pressure discussed above [Fig. 2b] lowers the energy of the Ni $3d_{x^2-y^2}$ orbital relative to the Ni $3d_{z^2}$ states [Fig. 5a]. This results in enhanced (reduced) DFT + U occupation numbers of the Ni $3d_{x^2-y^2}$ ($3d_{z^2}$) orbitals. These findings are consistent with recent reports based on a model study[52] and demonstrate explicitly that the orbital polarization can be tuned by external pressure. While the formal Ni$^{2.5+}$ ($d^{7.5}$) configuration implies that 1.5 electrons per Ni ion occupy the e_g manifold, the consistently higher values observed here highlight the involvement of the oxygen system, reminiscent of the $d^8\underline{L}$ configuration characteristic of rare-earth nickelates[32].

Finally, we find a Fermi surface with a quasi identical topology as in pressurized La$_3$Ni$_2$O$_7$ in Tb$_3$Ni$_2$O$_7$ at zero pressure [Fig. 5b], intriguingly *despite* the presence of pronounced octahedral rotations (space group *Cmc2$_1$*). We highlighted this compound already above due to its

considerably enhanced DOS at the Fermi energy and a concomitant strong involvement of the apical oxygen ions [Fig. 4a]. Therefore, we suggest this bilayer nickelate as a candidate for superconductivity at ambient pressure. Investigations of possible superconducting pairing in this system would be highly interesting.

Discussion

The structural and electronic properties of $A_3Ni_2O_7$ bilayer nickelates (A = La-Lu, Y, Sc) and their pressure dependence (0–150 GPa) were investigated by performing first-principles simulations including a Coulomb repulsion term, with particular emphasis on the role of orthorhombic distortion (b/a ratio), octahedral anisotropy, and octahedral rotations.

The lattice parameters were found to exhibit a highly anisotropic response to external pressure. Surprisingly, in $La_3Ni_2O_7$ at ~ 20 GPa, we observed an orthorhombic-to-tetragonal transition to an $I4/mmm$ phase at variance with recent XRD data, which points to yet unresolved complexities near the onset of superconductivity, e.g., electron- or hole-doped samples owing to variations in the oxygen stoichiometry. Due to the sensitivity of particularly the Ni $3d_{z^2}$-derived states and their energy relative to the Fermi level, this calls for a careful reassessment of the superconductivity mechanisms so-far proposed for the undoped compound. We showed that this transition coincides universally with vanishing octahedral tilts. The associated critical pressure increases quadratically over the rare-earth series, which we traced back to the enhancement of octahedral rotations with reducing A-site ionic radius. This establishes chemical and external pressure as two distinct control parameters in these complex oxides that independently and non-interchangeably allow the designing of their quantum state.

We compiled an ab initio structural phase diagram, which unveils two novel phases for A = Nd-Lu, Y, Sc at ambient conditions that are characterized by the emergence of significant in-plane c^+ octahedral rotations as well as in-plane bond disproportionations and exhibit a surprising pressure-driven electronic reconstruction involving the rotation of the Ni $3d_{z^2}$ orbital. The consecutive quenching of the distinct rotational degrees of freedom by pressure demonstrates that the potential energy landscape of the in-plane octahedral rotations is significantly shallower than for the octahedral tilts.

Moreover, we found unexpected correlations between T_c and the in-plane Ni-O-Ni bond angles for $La_3Ni_2O_7$, which determine the basal Ni $3d_{x^2-y^2}$-O $2p_{x,y}$ hybridization. An overall maximum near the onset of superconductivity indicates enhanced superexchange interactions and promotes the in-plane bond angles as an important aspect in understanding the superconductivity mechanism in bilayer rare-earth nickelates.

Finally, by disentangling the contributions of basal versus apical oxygen states at the Fermi level, we identified $Tb_3Ni_2O_7$ as an interesting candidate for superconductivity at ambient pressure, with a considerably higher DOS at the Fermi energy and a Fermi surface similar to pressurized $La_3Ni_2O_7$. This is even more astonishing since our results show that the perspectives of conventional chemical precompression are limited in this system. We suggest further exploration of the superconducting properties of $Tb_3Ni_2O_7$ at zero pressure.

This comprehensive study uncovers a profound tunability of the structural and electronic phases in this novel materials class. The richness of the structural phase diagram and the unexpected transitions identified specifically for the later rare-earth nickelates provide additional opportunities for the discovery of e.g. superconducting phases. It also emphasizes that future work needs to carefully assess the impact of defects, especially oxygen excess (hole doping) or oxygen vacancies (electron doping).

Methods

First-principles simulations

We performed first-principles simulations in the framework of density functional theory (DFT[81]) as implemented in the Vienna Ab initio Simulation Package[82,83], employing a wave-function cutoff of 520 eV. Exchange and correlations were described by using the generalized gradient approximation as parameterized by Perdew, Burke, and Ernzerhof[84]. The rare-earth $4f$ electrons were frozen in the core. We focus on the nonmagnetic phase here.

Additional results on the magnetic interactions, particularly our observation of ferromagnetic in-plane coupling (A-type antiferromagnetic ground state) and the proximity of an insulating site-disproportionate state, are discussed in the Supplementary Information[85–90]. Static correlation effects were considered within the DFT + U formalism[91,92], employing an effective U = 3 eV at the Ni sites, in line with previous nickelate work[9,10,19,27,77,78,90,93–95] and a recent analysis of the optical spectrum of $La_3Ni_2O_7$[96].

To account for octahedral rotations and in-plane bond disproportionations, the $A_3Ni_2O_7$ bilayer nickelates (A = La-Lu, Y, Sc) were modeled by using 24-atom unit cells. In this geometry, the Brillouin zone was sampled employing $8 \times 8 \times 8$ Monkhorst-Pack $\vec{k}$-point grids[97] in conjunction with a Gaussian smearing of 5 mRy. We confirmed that these parameters provide converged energies and lattice parameters. Accurate densities of states were obtained on $12 \times 12 \times 12$ $\vec{k}$-point grids. The compounds can equivalently be described by orthorhombic 48-atom unit cells [Fig. 1(a)]; for these, we used $8 \times 8 \times 2$ $\vec{k}$-point grids.

The lattice parameters a, b and c (given with respect to the more convenient orthorhombic representation in the following) and the internal ionic positions were accurately optimized in each case in DFT + U under zero and finite external pressure, reducing ionic forces below 1 mRy/a.u.

Data availability

The data is available upon reasonable request to the authors.

References

1. Sun, H. et al. Signatures of superconductivity near 80 K in a nickelate under high pressure. *Nature* **621**, 493–498 (2023).
2. Li, D. et al. Superconductivity in an infinite-layer nickelate. *Nature* **572**, 624–627 (2019).
3. Li, D. et al. Superconducting dome in $Nd_{1-x}Sr_xNiO_2$ infinite layer films. *Phys. Rev. Lett.* **125**, 027001 (2020).
4. Zeng, S. et al. Phase diagram and superconducting dome of infinite-layer $Nd_{1-x}Sr_xNiO_2$ thin films. *Phys. Rev. Lett.* **125**, 147003 (2020).
5. Nomura, Y. et al. Formation of a two-dimensional single-component correlated electron system and band engineering in the nickelate superconductor $NdNiO_2$. *Phys. Rev. B* **100**, 205138 (2019).
6. Jiang, P., Si, L., Liao, Z. & Zhong, Z. Electronic structure of rare-earth infinite-layer $RNiO_2$ (R = La, Nd). *Phys. Rev. B* **100**, 201106 (2019).
7. Sakakibara, H. et al. Model construction and a possibility of cupratelike pairing in a new d^9 nickelate superconductor $(Nd,Sr)NiO_2$. *Phys. Rev. Lett.* **125**, 077003 (2020).
8. Jiang, M., Berciu, M. & Sawatzky, G. A. Critical nature of the Ni spin state in doped $NdNiO_2$. *Phys. Rev. Lett.* **124**, 207004 (2020).
9. Botana, A. S. & Norman, M. R. Similarities and differences between $LaNiO_2$ and $CaCuO_2$ and implications for superconductivity. *Phys. Rev. X* **10**, 011024 (2020).
10. Geisler, B. & Pentcheva, R. Fundamental difference in the electronic reconstruction of infinite-layer versus perovskite neodymium nickelate films on $SrTiO_3(001)$. *Phys. Rev. B* **102**, 020502(R) (2020).
11. Lechermann, F. Late transition metal oxides with infinite-layer structure: nickelates versus cuprates. *Phys. Rev. B* **101**, 081110 (2020).
12. Wu, X. et al. Robust $d_{x^2-y^2}$-wave superconductivity of infinite-layer nickelates. *Phys. Rev. B* **101**, 060504 (2020).
13. Gu, Q. et al. Single particle tunneling spectrum of superconducting $Nd_{1-x}Sr_xNiO_2$ thin films. *Nat. Commun.* **11**, 6027 (2020).
14. Lu, H. et al. Magnetic excitations in infinite-layer nickelates. *Science* **373**, 213–216 (2021).
15. Ortiz, R. A. et al. Superlattice approach to doping infinite-layer nickelates. *Phys. Rev. B* **104**, 165137 (2021).
16. Lechermann, F. Doping-dependent character and possible magnetic ordering of $NdNiO_2$. *Phys. Rev. Mater.* **5**, 044803 (2021).

Article

17. Sahinovic, A. & Geisler, B. Active learning and element-embedding approach in neural networks for infinite-layer versus perovskite oxides. *Phys. Rev. Res.* **3**, L042022 (2021).

18. Wang, B. Y. et al. Isotropic Pauli-limited superconductivity in the infinite-layer nickelate $Nd_{0.775}Sr_{0.225}NiO_2$. *Nat. Phys.* **17**, 473–477 (2021).

19. Geisler, B. & Pentcheva, R. Correlated interface electron gas in infinite-layer nickelate versus cuprate films on $SrTiO_3$(001). *Phys. Rev. Res.* **3**, 013261 (2021).

20. Zeng, S. W. et al. Observation of perfect diamagnetism and interfacial effect on the electronic structures in infinite layer $Nd_{0.8}Sr_{0.2}NiO_2$ superconductors. *Nat. Commun.* **13**, 743 (2022).

21. Goodge, B. H. et al. Resolving the polar interface of infinite-layer nickelate thin films. *Nat. Mater.* **22**, 466–473 (2023).

22. Kreisel, A., Andersen, B. M., Rømer, A. T., Eremin, I. M. & Lechermann, F. Superconducting instabilities in strongly correlated infinite-layer nickelates. *Phys. Rev. Lett.* **129**, 077002 (2022).

23. Rossi, M. et al. A broken translational symmetry state in an infinite-layer nickelate. *Nat. Phys.* **18**, 869–873 (2022).

24. Fowlie, J. et al. Intrinsic magnetism in superconducting infinite-layer nickelates. *Nat. Phys.* **18**, 1043–1047 (2022).

25. Sahinovic, A. & Geisler, B. Quantifying transfer learning synergies in infinite-layer and perovskite nitrides, oxides, and fluorides. *J. Phys.: Condens. Matter* **34**, 214003 (2022).

26. Sahinovic, A., Geisler, B. & Pentcheva, R. Nature of the magnetic coupling in infinite-layer nickelates versus cuprates. *Phys. Rev. Mater.* **7**, 114803 (2023).

27. Geisler, B. Rashba spin-orbit coupling in infinite-layer nickelate films on $SrTiO_3$(001) and $KTaO_3$(001). *Phys. Rev. B* **108**, 224502 (2023).

28. Osada, M. et al. A superconducting praseodymium nickelate with infinite layer structure. *Nano Lett.* **20**, 5735–5740 (2020).

29. Osada, M. et al. Nickelate superconductivity without rare-earth magnetism: (La,Sr)NiO_2. *Adv. Mater.* **33**, 2104083 (2021).

30. Pan, G. A. et al. Superconductivity in a quintuple-layer square-planar nickelate. *Nat. Mater.* **21**, 160–164 (2022).

31. Lorenz, M. et al. The 2016 oxide electronic materials and oxide interfaces roadmap. *J. Phys. D: Appl. Phys.* **49**, 433001 (2016).

32. Middey, S. et al. Physics of ultrathin films and heterostructures of rare-earth nickelates. *Annu. Rev. Mater. Res.* **46**, 305–334 (2016).

33. Belviso, F. et al. Viewpoint: atomic-scale design protocols toward energy, electronic, catalysis, and sensing applications. *Inorg. Chem.* **58**, 14939–14980 (2019).

34. Geisler, B., Yordanov, P., Gruner, M. E., Keimer, B. & Pentcheva, R. Tuning the thermoelectric properties of transition metal oxide thin films and superlattices on the quantum scale. *Phys. Status Solidi* 2100270 (2021).

35. Wang, N. N. et al. Pressure-induced monotonic enhancement of tc to over 30 k in superconducting $Pr_{0.82}Sr_{0.18}NiO_2$ thin films. *Nat. Commun.* **13**, 4367 (2022).

36. Hou, J. et al. Emergence of high-temperature superconducting phase in pressurized $La_3Ni_2O_7$ crystals. *Chin. Phys. Lett.* **40**, 117302 (2023).

37. Zhang, Y. et al. High-temperature superconductivity with zero-resistance and strange metal behavior in $La_3Ni_2O_7$. Preprint at https://arxiv.org/abs/2307.14819 (2023).

38. Luo, Z., Hu, X., Wang, M., Wú, W. & Yao, D.-X. Bilayer two-orbital model of $La_3Ni_2O_7$ under pressure. *Phys. Rev. Lett.* **131**, 126001 (2023).

39. Gu, Y., Le, C., Yang, Z., Wu, X. & Hu, J. Effective model and pairing tendency in bilayer Ni-based superconductor $La_3Ni_2O_7$. Preprint at https://arxiv.org/abs/2306.07275 (2023).

40. Yang, Q.-G., Wang, D. & Wang, Q.-H. Possible $s_\pm$-wave superconductivity in $La_3Ni_2O_7$. *Phys. Rev. B* **108**, L140505 (2023).

41. Lechermann, F., Gondolf, J., Bötzel, S. & Eremin, I. M. Electronic correlations and superconducting instability in $La_3Ni_2O_7$ under high pressure. *Phys. Rev. B* **108**, L201121 (2023).

42. Sakakibara, H., Kitamine, N., Ochi, M. & Kuroki, K. Possible high T_c superconductivity in $La_3Ni_2O_7$ under high pressure through

43. manifestation of a nearly half-filled bilayer Hubbard model. *Phys. Rev. Lett.* **132**, 106002 (2024).

43. Shen, Y., Qin, M. & Zhang, G.-M. Effective bi-layer model hamiltonian and density-matrix renormalization group study for the high-T_c superconductivity in $La_3Ni_2O_7$ under high pressure. *Chin. Phys. Lett.* **40**, 127401 (2023).

44. Christiansson, V., Petocchi, F. & Werner, P. Correlated electronic structure of $La_3Ni_2O_7$ under pressure. *Phys. Rev. Lett.* **131**, 206501 (2023).

45. Shilenko, D. A. & Leonov, I. V. Correlated electronic structure, orbital-selective behavior, and magnetic correlations in double-layer $La_3Ni_2O_7$ under pressure. *Phys. Rev. B* **108**, 125105 (2023).

46. Liu, Z. et al. Electronic correlations and energy gap in the bilayer nickelate $La_3Ni_2O_7$. Preprint at https://arxiv.org/abs/2307.02950 (2023).

47. Wú, W., Luo, Z., Yao, D.-X. & Wang, M. Superexchange and charge transfer in the nickelate superconductor under pressure. Sci. China Phys. Mech. Astron. 67, 117402 (2024).

48. Cao, Y. & Yang, Y.-f Flat bands promoted by Hund's rule coupling in the candidate double-layer high-temperature superconductor $La_3Ni_2O_7$ under high pressure. *Phys. Rev. B* **109**, L081105 (2024).

49. Chen, X., Jiang, P., Li, J., Zhong, Z. & Lu, Y. Critical charge and spin instabilities in superconducting $La_3Ni_2O_7$. Preprint at https://arxiv.org/abs/2307.07154 (2023).

50. Liu, Y.-B., Mei, J.-W., Ye, F., Chen, W.-Q. & Yang, F. $s^\pm$-wave pairing and the destructive role of apical-oxygen deficiencies in $La_3Ni_2O_7$ under pressure. *Phys. Rev. Lett.* **131**, 236002 (2023).

51. Lu, C., Pan, Z., Yang, F. & Wu, C. Interlayer coupling driven high-temperature superconductivity in $La_3Ni_2O_7$ under pressure. Preprint at https://arxiv.org/abs/2307.14965 (2023).

52. Zhang, Y., Lin, L.-F., Moreo, A., Maier, T. A. & Dagotto, E. Structural phase transition, s ± -wave pairing, and magnetic stripe order in bilayered superconductor $La_3Ni_2O_7$ under pressure. *Nat. Commun.* **15**, 2470 (2024).

53. Oh, H. & Zhang, Y.-H. Type-II $t - J$ model and shared superexchange coupling from Hund's rule in superconducting $La_3Ni_2O_7$. *Phys. Rev. B* **108**, 174511 (2023).

54. Liao, Z. et al. Electron correlations and superconductivity in $La_3Ni_2O_7$ under pressure tuning. Preprint at https://arxiv.org/abs/2307.16697 (2023).

55. Qu, X.-Z. et al. Bilayer t-j-$j_\perp$ model and magnetically mediated pairing in the pressurized nickelate $La_3Ni_2O_7$. *Phys. Rev. Lett.* **132**, 036502 (2024).

56. Keimer, B., Kivelson, S. A., Norman, M. R., Uchida, S. & Zaanen, J. From quantum matter to high-temperature superconductivity in copper oxides. *Nature* **518**, 179–186 (2015).

57. Chubukov, A. & Hirschfeld, P. J. Iron-based superconductors, seven years later. *Phys. Today* **68**, 46–52 (2015).

58. Drozdov, A. P., Eremets, M. I., Troyan, I. A., Ksenofontov, V. & Shylin, S. I. Conventional superconductivity at 203 Kelvin at high pressures in the sulfur hydride system. *Nature* **525**, 73–76 (2015).

59. Drozdov, A. P. et al. Superconductivity at 250 K in lanthanum hydride under high pressures. *Nature* **569**, 528–531 (2019).

60. Hu, B. et al. Structure-property coupling in $Sr_3(Ru_{1-x}Mn_x)_2O_7$. *Phys. Rev. B* **84**, 174411 (2011).

61. Puetter, C. M., Rau, J. G. & Kee, H.-Y. Microscopic route to nematicity in $Sr_3Ru_2O_7$. *Phys. Rev. B* **81**, 081105 (2010).

62. Mesa, D. et al. Single-bilayer E-type antiferromagnetism in Mn-substituted $Sr_3Ru_2O_7$: neutron scattering study. *Phys. Rev. B* **85**, 180410 (2012).

63. Mukherjee, S. & Lee, W.-C. Structural and magnetic field effects on spin fluctuations in $Sr_3Ru_2O_7$. *Phys. Rev. B* **94**, 064407 (2016).

64. Nakayama, M. et al. Orbital-selective metal-insulator transition lifting the t_{2g} band hybridization in the hund metal $Sr_3(Ru_{1-x}Mn_x)_2O_7$. *Phys. Rev. B* **98**, 161102 (2018).

65. Mathieu, R. et al. Impurity-induced transition to a mott insulator in $Sr_3Ru_2O_7$. *Phys. Rev. B* **72**, 092404 (2005).

66. Zhang, Z., Greenblatt, M. & Goodenough, J. Synthesis, structure, and properties of the layered perovskite La₃Ni₂O₇−δ. *J. Solid State Chem.* **108**, 402–409 (1994).

67. Ling, C. D., Argyriou, D. N., Wu, G. & Neumeier, J. Neutron diffraction study of La₃Ni₂O₇: structural relationships among *n* = 1, 2, and 3 phases La$_{n+1}$Ni$_n$O$_{3n+1}$. *J. Solid State Chem.* **152**, 517–525 (2000).

68. Wang, L. et al. Structure responsible for the superconducting state in La₃Ni₂O₇ at high pressure and low temperature conditions. Preprint at https://arxiv.org/abs/2311.09186 (2023).

69. Taniguchi, S. et al. Transport, magnetic and thermal properties of La₃Ni₂O₇−δ. *J. Phys. Soc. Jpn.* **64**, 1644–1650 (1995).

70. Varignon, J., Grisolia, M. N., Íñiguez, J., Barthélémy, A. & Bibes, M. Complete phase diagram of rare-earth nickelates from first-principles. *npj Quantum Mater.* **2**, 21 (2017).

71. Catalano, S. et al. Rare-earth nickelates *R*NiO₃: thin films and heterostructures. *Rep. Prog. Phys.* **81**, 046501 (2018).

72. Geisler, B. & Pentcheva, R. Competition of defect ordering and site disproportionation in strained LaCoO₃ on SrTiO₃(001). *Phys. Rev. B* **101**, 165108 (2020).

73. Radhakrishnan, P. et al. Orbital engineering in YVO₃-LaAlO₃ superlattices. *Phys. Rev. B* **104**, L121102 (2021).

74. Radhakrishnan, P. et al. Coupling of electronic and structural degrees of freedom in vanadate superlattices. *Phys. Rev. B* **105**, 165117 (2022).

75. Zhang, Y., Lin, L.-F., Moreo, A., Maier, T. A. & Dagotto, E. Trends in electronic structures and s$_±$-wave pairing for the rare-earth series in bilayer nickelate superconductor *R*₃Ni₂O₇. *Phys. Rev. B* **108**, 165141 (2023).

76. Wu, M. et al. Strain and composition dependence of orbital polarization in nickel oxide superlattices. *Phys. Rev. B* **88**, 125124 (2013).

77. Geisler, B. & Pentcheva, R. Inducing *n*- and *p*-type thermoelectricity in oxide superlattices by strain tuning of orbital-selective transport resonances. *Phys. Rev. Appl.* **11**, 044047 (2019).

78. Geisler, B., Follmann, S. & Pentcheva, R. Oxygen vacancy formation and electronic reconstruction in strained LaNiO₃ and LaNiO₃/LaAlO₃ superlattices. *Phys. Rev. B* **106**, 155139 (2022).

79. Iliev, M. N. et al. Raman spectroscopy of orthorhombic perovskitelike YMnO₃ and LaMnO₃. *Phys. Rev. B* **57**, 2872–2877 (1998).

80. Baldini, M. et al. Origin of colossal magnetoresistance in LaMnO₃ manganite. *Proc. Natl. Acad. Sci. USA* **112**, 10869–10872 (2015).

81. Kohn, W. & Sham, L. J. Self-consistent equations including exchange and correlation effects. *Phys. Rev.* **140**, A1133–A1138 (1965).

82. Kresse, G. & Joubert, D. From ultrasoft pseudopotentials to the projector augmented-wave method. *Phys. Rev. B* **59**, 1758–1775 (1999).

83. Blöchl, P. E. Projector augmented-wave method. *Phys. Rev. B* **50**, 17953–17979 (1994).

84. Perdew, J. P., Burke, K. & Ernzerhof, M. Generalized gradient approximation made simple. *Phys. Rev. Lett.* **77**, 3865–3868 (1996).

85. Choi, M.-Y., Lee, K.-W. & Pickett, W. E. Role of 4*f* states in infinite-layer NdNiO₂. *Phys. Rev. B* **101**, 020503 (2020).

86. Liu, Z. et al. Evidence for charge and spin density waves in single crystals of La₃Ni₂O₇ and La₃Ni₂O₆. *Sci. China Phys. Mech. Astron.* **66**, 217411 (2022).

87. Chen, K. et al. Evidence of spin density waves in La₃Ni₂O₇−δ. Preprint at https://arxiv.org/abs/2311.15717 (2023).

88. Fukamachi, T., Kobayashi, Y., Miyashita, T. & Sato, M. ¹³⁹La NMR studies of layered perovskite systems La₃Ni₂O₇−δ and La₄Ni₃O₁₀. *J. Phys. Chem. Solids* **62**, 195–198 (2001).

89. Blanca-Romero, A. & Pentcheva, R. Confinement-induced metal-to-insulator transition in strained LaNiO₃/LaAlO₃ superlattices. *Phys. Rev. B* **84**, 195450 (2011).

90. Geisler, B. & Pentcheva, R. Confinement- and strain-induced enhancement of thermoelectric properties in LaNiO₃/LaAlO₃(001) superlattices. *Phys. Rev. Mater.* **2**, 055403 (2018).

91. Liechtenstein, A. I., Anisimov, V. I. & Zaanen, J. Density-functional theory and strong interactions: orbital ordering in Mott-Hubbard insulators. *Phys. Rev. B* **52**, R5467 (1995).

92. Dudarev, S. L., Botton, G. A., Savrasov, S. Y., Humphreys, C. J. & Sutton, A. P. Electron-energy-loss spectra and the structural stability of nickel oxide: An LSDA + U study. *Phys. Rev. B* **57**, 1505 (1998).

93. Liu, J. et al. Heterointerface engineered electronic and magnetic phases of NdNiO₃ thin films. *Nat. Commun.* **4**, 2714 (2013).

94. Geisler, B., Blanca-Romero, A. & Pentcheva, R. Design of *n*- and *p*-type oxide thermoelectrics in LaNiO₃/SrTiO₃(001) superlattices exploiting interface polarity. *Phys. Rev. B* **95**, 125301 (2017).

95. Wrobel, F. et al. Digital modulation of the nickel valence state in a cuprate-nickelate heterostructure. *Phys. Rev. Materials* **2**, 035001 (2018).

96. Geisler, B. et al. Optical properties and electronic correlations in La₃Ni₂O₇ bilayer nickelates under high pressure. Preprint at https://arxiv.org/abs/2401.04258 (2024).

97. Monkhorst, H. J. & Pack, J. D. Special points for Brillouin-zone integrations. *Phys. Rev. B* **13**, 5188 (1976).

Acknowledgements

Author contributions

B.G. and P.J.H. conceived of the project. J.J.H., G.R.S., R.G.H. and P.J.H. supervised the research. B.G. performed the theoretical simulations and corresponding analysis. B.G. and P.J.H. wrote the manuscript. All authors discussed the results and revised the manuscript.

Competing interests

The authors declare no competing interests.

Additional information

Supplementary information The online version contains supplementary material available at https://doi.org/10.1038/s41535-024-00648-0.

Correspondence and requests for materials should be addressed to Benjamin Geisler.

Reprints and permissions information is available at http://www.nature.com/reprints

Publisher's note Springer Nature remains neutral with regard to jurisdictional claims in published maps and institutional affiliations.